

Quantitative corrosion imaging of pipelines using multi helical guided ultrasonic waves

Ehsan Dehghan-Niri¹ and Salvatore Salamone^{*2}

¹Department of Civil, Structural and Environmental Engineering, University at Buffalo, USA

²Department of Civil, Architectural and Environmental Engineering, University of Texas at Austin,
301 E Dean Keeton, C1748, Austin, TX, 78712, USA

(Received December 28, 2015, Revised April 4, 2016, Accepted May 3, 2016)

Abstract. This paper presents a multi helical ultrasonic imaging approach for quantitative corrosion damage monitoring of cylindrical structures. The approach consists of two stages. First a multi helical ultrasonic imaging (MHUI) algorithm is used to provide qualitative images of the structure of interest. Then, an optimization problem is solved in order to obtain quantitative damage information, such as thickness map. Experimental tests are carried out on a steel pipe instrumented with six piezoelectric transducers to validate the proposed approach. Three thickness recesses are considered to simulate corrosion damage. The results show the efficiency of the proposed approach for quantifying corrosion location, area and remnant thickness.

Keywords: corrosion; guided waves; imaging algorithms

1. Introduction

Corrosion is the leading cause of pipeline, pressure vessels, and storage tanks failures (Brondel *et al.* 1994). In order to reduce the maintenance costs and to increase the safety of these structures, researchers and practitioners are increasingly interested in improving current nondestructive evaluation (NDE) technologies or developing advanced structural health monitoring (SHM) strategies (Lu and Michaels 2005). In particular, SHM strategies based on guided ultrasonic waves (GUW) and imaging reconstruction algorithms, have received significant interest in the last few years (Hall *et al.* 2011, Jansen and Hutchin 1990, Hinders *et al.* 1998, Huthwaite and Simonetti 2013, Willey *et al.* 2014, Belanger *et al.* 2010, Huthwaite *et al.* 2013, Gao *et al.* 2005, Zhao *et al.* 2007, Flynn *et al.* 2011, Ciampa *et al.* 2014, Dehghan-Niri and Salamone 2014, Pierce and Kil 1990, Li and Rose 2006, Leonard and Hinders 2003, Qing *et al.* 2009, Leonard and Hinders 2005). In general, GUW-based imaging methods generate an intensity map of the structure of interest, in which the largest intensity, or brightest pixels, identify the damage location(s) (Hall *et al.* 2011). For instance, a Lamb wave tomography approach was used by Jansen and Hutchin (1990), and then by Hinders *et al.* (1998) to reconstruct the spatial distribution of thickness loss in plate-like structures. A hybrid algorithm for breast ultrasound tomography was used by Huthwaite and Simonetti (2013) to generate thickness mapping of plate structures.

*Corresponding author, Professor, E-mail: salamone@utexas.edu

Leonard and Hinders (2003) applied a G UW tomography approach to locate and size flaws in pipes. They anticipated that the accuracy of guided wave tomography could be improved by exploiting the information contained in higher-order helical modes. A general inversion method was proposed by Willey *et al.* (2014) to improve the accuracy of the reconstructed images by using information extracted from higher-order helical modes (up to the second helical order). They used electromagnetic acoustic transducers (EMATs) to generate and receive helical modes. A low frequency guided wave diffraction tomography algorithm was developed by Belanger *et al.* (2010) to generate thickness mapping in pipes. Recently Huthwaite *et al.* (2013) have presented a detailed study on the advantages and disadvantages of the two fundamental Lamb waves modes (S_0 and A_0) for guided wave tomography applications. Although these guided wave tomography approaches have seen significant developments, a large sensor density is usually required in order to obtain a high resolution image.

In order to reduce the number of sensors, as well as to exploit the potential advantages of guided wave tomography for SHM applications, imaging methods based on sparse arrays (i.e., spatially distributed) of ultrasonic sensors have been recently investigated (Gao *et al.* 2005, Zhao *et al.* 2007, Flynn *et al.* 2011, Ciampa *et al.* 2014, Dehghan-Niri and Salamone 2014), including the Reconstruction Algorithm for the Probabilistic Inspection Damage (RAPID) (Gao *et al.* 2005, Zhao *et al.* 2007), Rayleigh Maximum Likelihood Estimator (RMLE) (Flynn *et al.* 2011), and nonlinear elastic wave imaging algorithms (Ciampa *et al.* 2014). Dehghan-Niri and Salamone (2014) have proposed a Multi Helical Ultrasonic Imaging (MHUI) method which exploits high-order helical guided waves (up to the ninth order) to artificially increase the ray density/resolution without increasing the number of sensors. In that work the RAPID algorithm has been modified to include information associated with the different helical paths. Although these methods can mitigate the sensor density problem, they cannot provide any quantitative information on the extent of the corrosion (e.g., wall thickness map). This paper extends the MHUI method developed in Dehghan-Niri and Salamone (2014) to provide quantitative information on the corrosion damage such as location, size and remnant thickness.

This paper is organized as follow. In section 2 the MHUI is briefly summarized. The corrosion quantification approach is presented in section 3. Experimental tests and results are discussed in section 4. Finally concluding remarks are provided in section 5.

2. Multi Helical Ultrasonic Imaging (MHUI)

This section provides a brief summary of the multi-helical ultrasonic imaging (MHUI). The reader is referred to Dehghan-Niri and Salamone (2014) for a more in-depth discussion, including implementation details. Let's consider a cylindrical structure instrumented with a pair of transmitting/receiving (S_i/S_j) transducers as shown in Fig. 1. Circumferential waves can propagate from S_i to S_j through an infinite number of helical paths (Dehghan-Niri and Salamone 2014, Pierce and Kil 1990, Li and Rose 2006). The " h -th order" helical path indicates the h -th longest path between a transducer pair, (the first three helical orders are shown in Fig. 1(a)). For small wall thickness-to-diameter-ratios, these waves can be treated as Lamb waves propagating through an equivalent unwrapped plate, as shown in Fig. 1(b). Using the unwrapped representation, each helical wave can be considered as a single waveform detected by virtual transducers placed at vertically repeating positions (Leonard KR, Hinders 2003). The vertical distance between each pair of virtual transducers is $n_h D$, where D is the diameter of the cylinder, and

$N_h = 0, -1, +1, -2, +2, \dots, -\infty, +\infty$. Given a transducer pair located at coordinates (x_i, y_i) and (x_j, y_j) , the length of the h -th order helical path l_h can be calculated as

$$l_h = \sqrt{(L)^2 + (B + n_h \pi D)^2} \quad N_h = 0, -1, +1, -2, +2, \dots, -\infty, +\infty \quad (1)$$

where $L = |x_j - x_i|$ and $B = |y_j - y_i|$. Without loss of generality the theoretical cut line to unwrap the cylinder can be chosen to satisfy the inequality $B \leq \pi D / 2$. Eq. (1) represents a set of lengths (l_h) sorted from the smallest path l_1 to the largest path l_h associated to the first and to the h -th helical orders.

The time of arrival $T_{kh}^{(m)}$ of each helical Lamb-like mode depends upon its group velocity $V^{(m)}$, and path's length an can be determined as

$$T_{kh}^{(m)} = \frac{l_{kh}}{V^{(m)}} \quad (2)$$

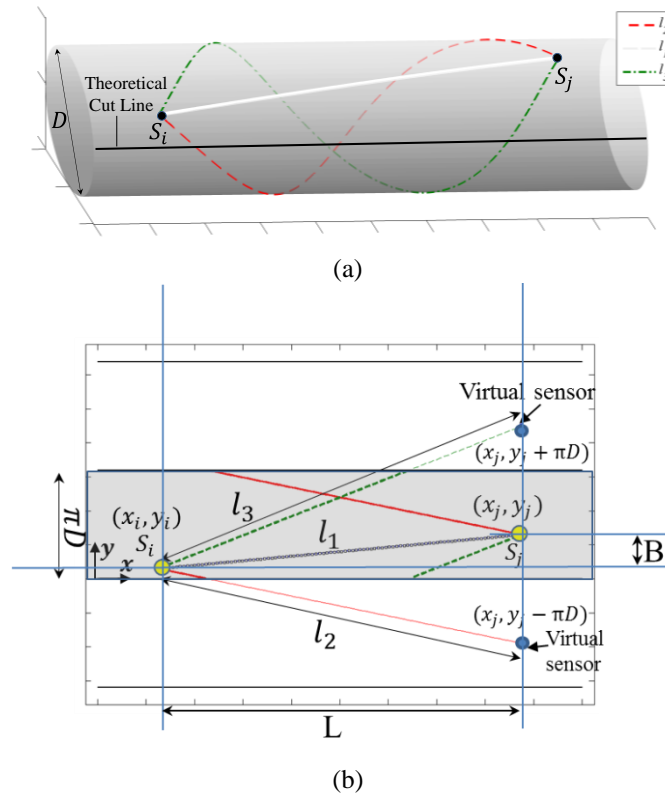


Fig. 1 The first three shortest helical paths: (a) 3-D view and (b) unwrapped cylinder (Cartesian coordinates)

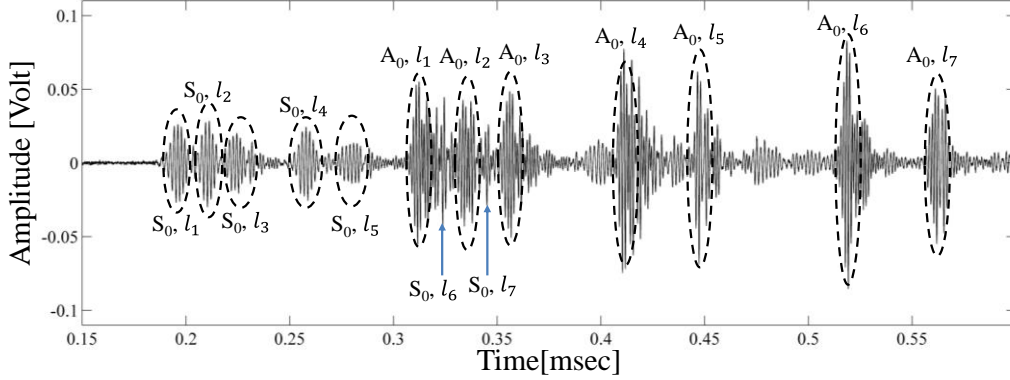


Fig. 2 The signals received from the transmitter/receiver pair # 1 for a pristine condition (baseline)

where the superscript m is used to indicate the specific Lamb wave mode propagating along the h -th helical path of k -th transducer pair. As per Eq. (2), the time of arrival $T_{kh}^{(m)}$ of each helical mode can be controlled by the relative position of the transducer pairs (x_i, y_i) and (x_j, y_j) , and group wave velocity $V^{(m)}$.

For illustrative purposes, Fig. 2 shows a typical signal received from a transducer used in the experiment described in Section IV. Two set of wave packets can be identified corresponding to the S_0 and A_0 mode. Each wave packet contains damage information of the helical path through which it propagates. It can be observed that multiple helical paths can be inspected with only a pair of transmitter/receiver. A modified probabilistic reconstruction algorithm (MPRA) was used to take into the account the contribution of different helical paths.

The MPRA has many practical advantages, including flexibility in array geometry selection and, most importantly, it enables a reconstruction to be performed with high reconstruction quality and fast speed. The method uses prerecorded baseline signals, measured while the structure is in a pristine state (i.e., damage-free). Differential signals (i.e., subtraction of baseline signals from subsequently measured signals) are used to isolate the effects of damage introduced between two measurements. The normalized root mean square of the gated differential signals is used as a damage-sensitive feature, that is

$$w_{kh}^{(m)} = \frac{\int_{T_{kh}^{(m)}}^{T_{kh}^{(m)} + \Delta t} [S_k(t) - H_k(t)]^2 dt}{\int_{T_{kh}^{(m)}}^{T_{kh}^{(m)} + \Delta t} [S_k(t)]^2 dt} \quad (3)$$

where $S_k(t)$ and $H_k(t)$ are the baseline and the current signal, respectively. Δt is the excitation pulse duration. $T_{kh}^{(m)}$ is the arrival time of h -th helical order packets of the m -th Lamb wave mode of k -th transducer pair used for image reconstruction and can be calculated from Eq. (2). The damage-sensitive features $w_{kh}^{(m)}$ are extracted from the differential signals of N_h helical

orders measured by N independent pairs of transducers. Conventionally full sets of N pairwise transducer signals are acquired by exciting one transducer at a time in a round-robin fashion. In general N_h unique features associated with N_h helical paths are extracted from each independent pair of transducers (i.e., seven pieces of information related to A_0 and/or S_0 mode can be extracted from transmitted signals of transducer pair 1 shown in Fig. 2). Extracting N_h pieces of information from each signal significantly increase the number of paths that can be inspected, from N (Huthwaite and Simonetti 2013, Belanger *et al.* 2008, Leonard and Hinders 2003, Qing *et al.* 2009, Leonard and Hinders 2005, Nagy *et al.* 2014, Leonard and Hinders 2005) to $N \times N_h$ Dehghan-Niri and Salamone (2014).

The MPRA algorithm combines the damage sensitive features associated with all helical orders of all transducer pairs as

$$I(x, y) = \sum_{k=1}^N \sum_{h=1}^{N_h} p_{kh}(x, y) = \eta \sum_{k=1}^N \sum_{h=1}^{N_h} w_{kh}^{(m)} \frac{\gamma_h - R_{kh}(x, y)}{\gamma_h - 1} \tag{4}$$

where $I(x, y)$ is the image intensity which estimate the defect probability at the location (x, y) in the unwrapped configuration within the reconstruction region, and $p_{kh}(x, y)$ is the probability associated to the k -th transducer pair and h -th helical order. N is the total number of independent transmitting and receiving pairs in a network of n_s transducers. N_h is the maximum helical order used in the imaging algorithm. η is a probability scaling factor used to make the maximum probability or image intensity equal to one. γ is a scaling parameter which controls the size of the effective elliptical distribution area, where $\gamma > 1$. Special care should be taken in defining the γ because, if γ is too small then artifacts will be introduced and if γ is too large, the resolution will be lost. Furthermore, a large value for γ may result in artifacts due to unwanted overlap of elliptical areas for the high helical orders. This problem was addressed in¹⁴, by setting the value of γ as an inverse function of helical order h

$$\gamma_h = 1 + \frac{\nu}{h} \tag{5}$$

The value of ν was determined by trial-and-error and set to 0.025. For the k -th pair and h -th helical order, R_{kh} is calculated in the unwrapped representation as

$$R_{kh}(x, y) = \frac{\sqrt{(x - x_{1k})^2 + (y - y_{1k})^2} + \sqrt{(x - x_{2kh})^2 + (y - y_{2kh})^2}}{\sqrt{(x_{1k} - x_{2kh})^2 + (y_{1k} - y_{2kh})^2}} \tag{6}$$

where (x_{1k}, y_{1k}) and (x_{2kh}, y_{2kh}) are the transmitter and virtual receiver coordinates, respectively. The contours of the distribution estimation are a set of ellipses with the two focal points being the transmitting and the virtual receiver for each pair, e.g., there are N_h ellipses for each pair of transducers. A set of helical waves of transmitting/receiving pair signals that travel through the damage area are more affected by the defect than others. As a result, in the defect distribution probability image, the pixel at the defect location has a larger pixel intensity/probability than other pixels. The reconstruction of the final image is the accumulation

and transformation of the constructed image from the artificial plates in the unwrapped coordinate system to the single unwrapped plate.

The operational frequency of the MHUI algorithm should be selected within the shaded region shown in Fig. 3 for the following reasons Dehghan-Niri and Salamone (2014): i) GUW in a pipe can be treated as Lamb waves (Li and Rose 2006); ii) just the two fundamental Lamb wave modes (i.e., A_0 and S_0) can propagate, and iii) the group wave velocity remains almost constant, while the phase velocity is still dispersive enough to make the damage index in (3) very sensitive to thickness changes (Dehghan-Niri and Salamone 2014, Li and Rose 2006). Other advantages of using constant group velocity (CGV) operation point have been discussed by Nagy *et al.* (2014).

3. Corrosion patch quantification

Let's consider a corrosion patch in the unwrapped plate as shown in Fig. 4(a). Fig. 4(b) shows the corresponding reconstructed image $I(x, y)$ obtained by the MHUI algorithm. The proposed method to estimate the patch boundary $\Gamma(x, y)$ along with its thickness map, assumes the validity of the ray theory. For the ray theory to be valid, the characteristic size of the defect must be larger than the wavelength (L_f), and larger than the width (L_f) of the first Fresnel zone which can be approximated, in the middle of the ray path, as (Leonard and Hinders 2005, Belanger and Cawley 2009, Belanger 2009)

$$L_f\left(\frac{l}{2}\right) = \sqrt{l\lambda} \quad (7)$$

where l is the length of the ray path between a pair of transducer. Two additional assumptions are made in this paper: (i) scattering effects are neglected, and (ii) thickness changes are uniform within the corrosion patch area. Also for simplicity we assume that only a single defect is present.

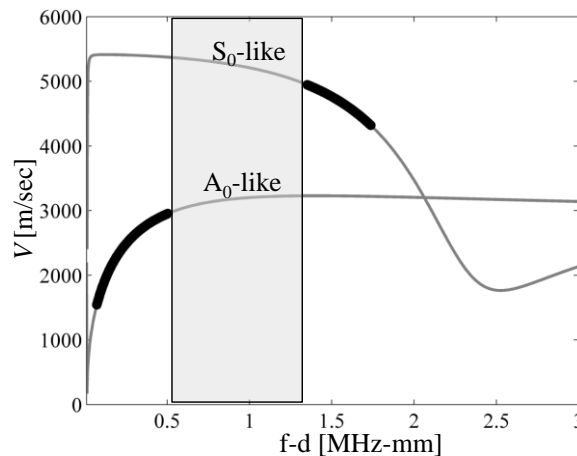
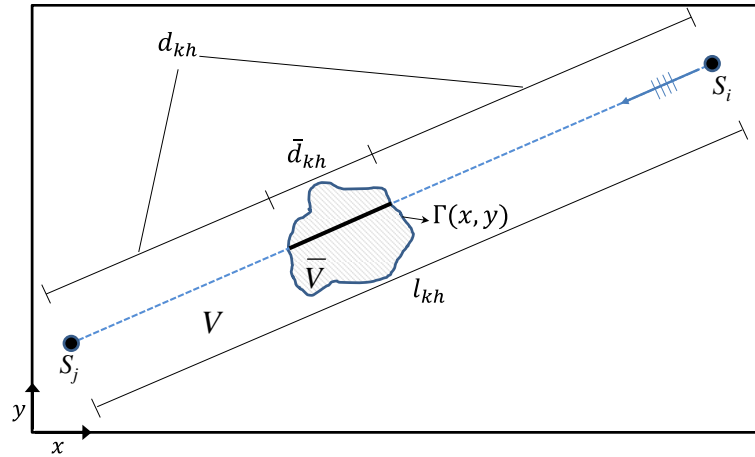
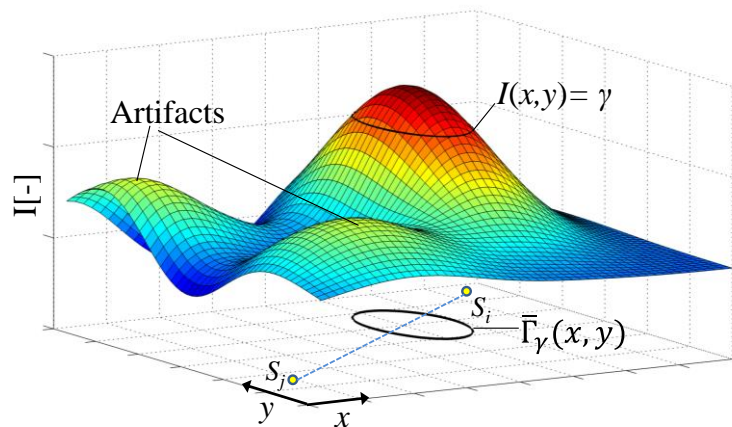


Fig. 3 Wave velocity dispersion curvature of 152 mm diameter steel pipe with 2.1 mm thickness. The shaded area corresponds to the frequency range to be used in the imaging stage and the black parts on the A_0 and S_0 modes corresponding to the frequency range to be used in the quantitative stage



(a)



(b)

Fig. 4 Schematic of (a) a corrosion patch and a pair of transducers in the unwrapped coordinates (b) assumed reconstructed image associated with the corrosion patch

Thickness mapping using time-of-flight straight ray tomography algorithms largely depends on the selection of the operational frequency. This frequency should be selected below the first cut-off frequency, to make sure the higher modes do not contaminate the signals, and within a frequency range in which the dispersion of the two fundamental modes (A_0 and S_0) is significant. A review of the operational frequency selection is presented in (Belanger and Cawley 2008). The paper shows that if the operational frequency is selected below the first cut-off frequency, there are two likely regions of operation for A_0 and S_0 , which are shown in Figure 3 with solid black lines. The A_0 mode, however is more sensitive to thickness changes, therefore, in this paper just the A_0 mode is considered.

Because of the dispersive nature of A_0 mode in the region shown in Fig. 3, the wave velocity changes as it propagates in the corrosion patch with boundary $\Gamma(x, y)$. If the boundary $\Gamma(x, y)$

can be approximated with one unique contour of the image, defined as $I(x, y) = \gamma$, then the problem of finding $\Gamma(x, y)$ can be reduced to the estimation of the counter level γ whose boundary is $\bar{\Gamma}_\gamma(x, y)$, as shown in Fig. 4(b). To estimate the wave velocity (\bar{V}) in the corrosion area, let's consider a transmitter (S_i) and a receiver (S_j) associated with the k -th transmitter/receiver pair, as shown in Fig. 4(a). The total travel time T_{kh} from the transmitter S_i to receiver S_j through the h -th helical path is defined in Eq. (2) (V is the wave velocity in the pristine structure). After the initiation of the corrosion process, the wave velocity in the corrosion patch changes to \bar{V} and the travel time change accordingly as

$$\bar{T}_{kh} = \frac{\bar{d}_{kh}}{\bar{V}} + \frac{d_{kh}}{V} \quad (8)$$

where \bar{d}_{kh} and d_{kh} are the portion of the helical inside and outside of corrosion patch respectively (see Fig. 4(a)). Having the image information $I(x, y)$, and based on the assumption that $\Gamma(x, y)$ can be approximated by $\bar{\Gamma}_\gamma(x, y)$, \bar{d}_{kh} and d_{kh} lengths can be calculated for different contour levels γ . The time difference in the total travel time before and after corrosion can be defined as

$$\Delta T_{kh} = \bar{T}_{kh} - T_{kh} \quad (9)$$

It should be noted that since the A_0 mode is used, a reduction in wave velocity V (see Fig. 3) is expected, and thus an increasing in the total travel time T_{kh} (i.e., ΔT_{kh} is positive).

The total helical path length l_{kh} in Eq. (1) is equal to

$$l_{kh} = d_{kh} + \bar{d}_{kh} \quad (10)$$

Substituting (2) (8) and (10) in (9) the time differences ΔT_{kh} can be calculated for different contour level γ and wave velocity \bar{V} as

$$\Delta T_{kh} = \bar{d}_{kh} \left(\frac{1}{\bar{V}} - \frac{1}{V} \right) \quad (11)$$

The actual time differences $\overline{\Delta T}_{kh}$ associated with the h -th helical order of k -th transducers pair can be experimentally measured by signals $S_k(t)$ and $H_k(t)$ received from a pristine and damaged condition, respectively. A common method to estimate the time of arrival difference $\overline{\Delta T}_{kh}$ is by using a cross correlation technique between the windowed signals ($S_k(t)$ and $H_k(t)$)

$$z_{kh}(\tau) = \frac{1}{\Delta t} \int_{T_{kh}^{(m)}}^{T_{kh}^{(m)} + \Delta t} S_k(t) H_k(t + \tau) dt \quad (12)$$

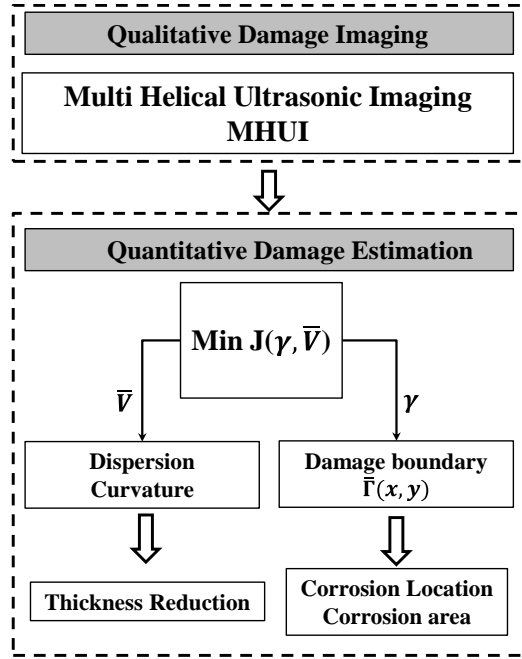


Fig. 5 Flowchart describing the proposed quantitative corrosion imaging approach

where Δt is the excitation pulse duration, and $T_{kh}^{(m)}$ is defined in Eq. (2). Having the measured time differences in Eq. (12) and the theoretical ones from Eq. (11) a weighted least square minimization problem is proposed in order to estimate the contour level γ and wave velocity \bar{V} as

$$\min J(\gamma, \bar{V}) = \sum_{k=1}^N \sum_{h=1}^{N_h} (\Delta T_{kh} - \overline{\Delta T}_{kh})^2 w_{kh} \delta_{\overline{\Delta T}_{kh} > 0} \tag{13}$$

where N is the number of independent transducer pairs, and N_h is the number of helical orders used in the image reconstruction. In Eq. (13) the w_{kh} is the damage index given in (3) and $\delta_{\overline{\Delta T}_{kh} > 0}$ is an indicator function defined as

$$\delta_{\overline{\Delta T}_{kh} > 0} = \begin{cases} 1 & \text{if } \overline{\Delta T}_{kh} > 0 \\ 0 & \text{if } \overline{\Delta T}_{kh} \leq 0 \end{cases} \tag{14}$$

The indicator function eliminates the error components with positive time delay. As discussed in (Belanger and Cawley 2009), if the Fresnel zone is not much smaller than the damage size (the first condition of the straight ray theory) thickness changes may cause an increasing in wave velocity of A_0 (see Fig. 5 in (Belanger and Cawley 2009)). The higher the helical order the larger is the helical path between a pair of transducers, and thus according to Eq. (7) the value of the first

Fresnel zone is large for high helical orders. As a result the proposed method does not satisfy the first condition of the straight ray theory. To overcome this issue, these error components were eliminated from the least square objective function in Eq. (13). Furthermore, the weighting component w_{kh} was introduced to increase the weight/contribution of the helical paths with higher damage index. The reason for this weighting is to increase the contribution of error components associated with the helical paths that are more likely to travel through the corrosion patch. It is worth noting that the objective function in Eq. (13) is not in parametric form so that the gradient based optimization method cannot be easily used. Several derivative free algorithms have been developed for minimizing an objective function such as the Eq. (13), including Genetic Algorithms (GA) (Dehghan-niri *et al.* 2010), Particle Swarm Optimization (PSO), and Mesh Grid Optimization (MGO) or coordinate search (Kolda *et al.* 2003). In this paper, a MGO algorithm was used, with 0.001 and 5 m/sec increments for γ and \bar{V} respectively. Therefore, the values of γ and \bar{V} were estimated by evaluating the objective function in Eq. (13) at gridded parameters. The correspond absolute minimum value represents the unknowns γ and \bar{V} . Overall the proposed quantitative corrosion imaging approach is shown in Fig. 5. It consists of two main stages. In the first stage a qualitative image is reconstructed using the MHUI algorithm. In the second stage, quantitative information (i.e., location, area and thickness) are estimated by solving an optimization problem.

4. Results

In order to validate the proposed algorithm, experiments were carried out on a 3000 mm long steel pipe with a 152.4 mm diameter and 2.1 mm thickness. Six piezoelectric disks with 5 mm diameter were attached to the surface of the pipe using a Loctite instant adhesive. To avoid reflections from the pipe ends, only the 2000 mm middle section of the pipe was instrumented (sensor density is transducers/area=6.4 Number/[m²]). Signal generation and data acquisition were achieved with a National Instruments (NI), modular PXI 1042 unit. This unit included an arbitrary waveform generator card (PXI 5411) and one, 20GS/s 12-bit multi-channel digitizers (PXI 5105). A high voltage amplifier was used to amplify the excitation to the ultrasonic transmitters, while each sensor was connected to a 40dB preamplifier. A 5-cycles ultrasonic toneburst with center frequency of 700 kHz corresponding to 1.47 MHz-mm (wavelength $\lambda=3.7$ mm) was used as excitation frequency in the MHUI algorithm (i.e., Qualitative damage imaging stage). This frequency was selected to meet the requirements described in section II, that is, below the first cut-off frequency (1.6 MHz-mm), and in a frequency range in which A_0 wasn't significantly dispersive (i.e., shaded region shown in Fig. 3). The center frequency selected to quantify the extent of corrosion (i.e., Quantitative damage estimation stage) was 240 kHz that corresponds to 0.50 MHz-mm (wavelength $\lambda=7.91$ mm).

Fig. 6 shows a schematic view of the experimental set-up in the unwrapped equivalent plate. Three thickness recesses were engineered to simulate corrosion damage. The in-plane dimensions of the defects were, $30\text{ mm} \times 40\text{ mm}$, $30\text{ mm} \times 80\text{ mm}$, and $60\text{ mm} \times 80\text{ mm}$, with depth equal to 40% of the pipe's wall thickness, as shown in Figure 7. It should be noted that the wavelength for the A_0 mode at the excitation frequency in the second stage is much smaller, than the smallest damage size (i.e., $7.91 \ll 30$). This value satisfies the second condition of the straight ray theory. However, the wavelength, particularly in the quantitative stage, does not strictly satisfy the ray

theory in which the damage size should be less than the first Fresnel zone in Eq. (7) of all helical paths. For example, the width of the first Fresnel zone of first helical order for transducer pairs 1-3 is 89 mm ($\sqrt{1003.1 \times 7.9} = 89 > 30$). The effect of this problem can be to some extent compensated by eliminating the error components with positive delay value in Eq. (13).

The sensor placement was discussed in details in (Dehghan-Niri and Salamone 2014). According to that paper the number of unambiguous independent transducers pairs in our network was $N=12$; these pairs are listed in Table 1. The maximum number of helical orders N_h used in the proposed imaging algorithm was set to nine. The corresponding ray coverage area is shown in Fig. 8. Extracting more data associated with multiple helical paths in MHUI from a received signal allows multiple lines to be inspected between a single transducer pair instead of only a single line, as is traditionally inspected between two transducers; therefore a large coverage can be achieved without increasing the number of transducers.

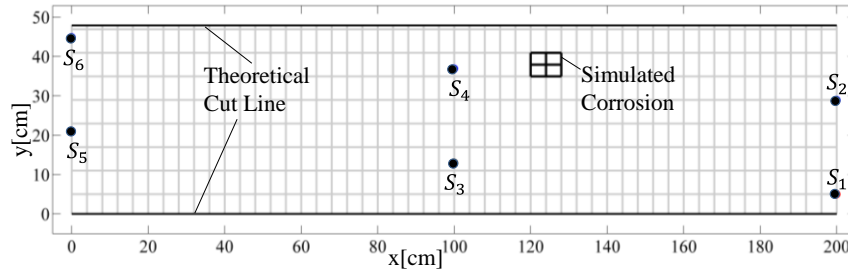


Fig. 6 Schematic view of the sensor network in the unwrapped equivalent plate view

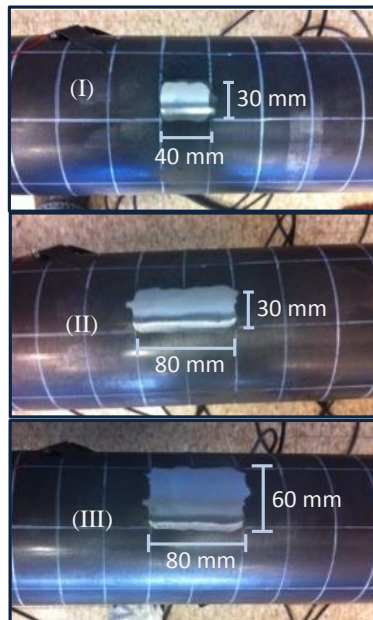


Fig. 7 Simulated corrosion patches

The image reconstruction results obtained using MHUI for the corrosion case I, II and III are shown in Fig. 9. These qualitative images will be used for quantifying the corrosion patch as discussed in Section III.

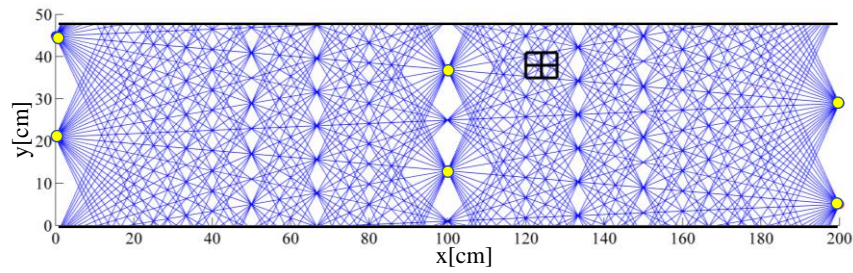


Fig. 8 All possible helical paths of 12 transmitter/receiver pair for ninth helical order, in the “unwrapped” plate view

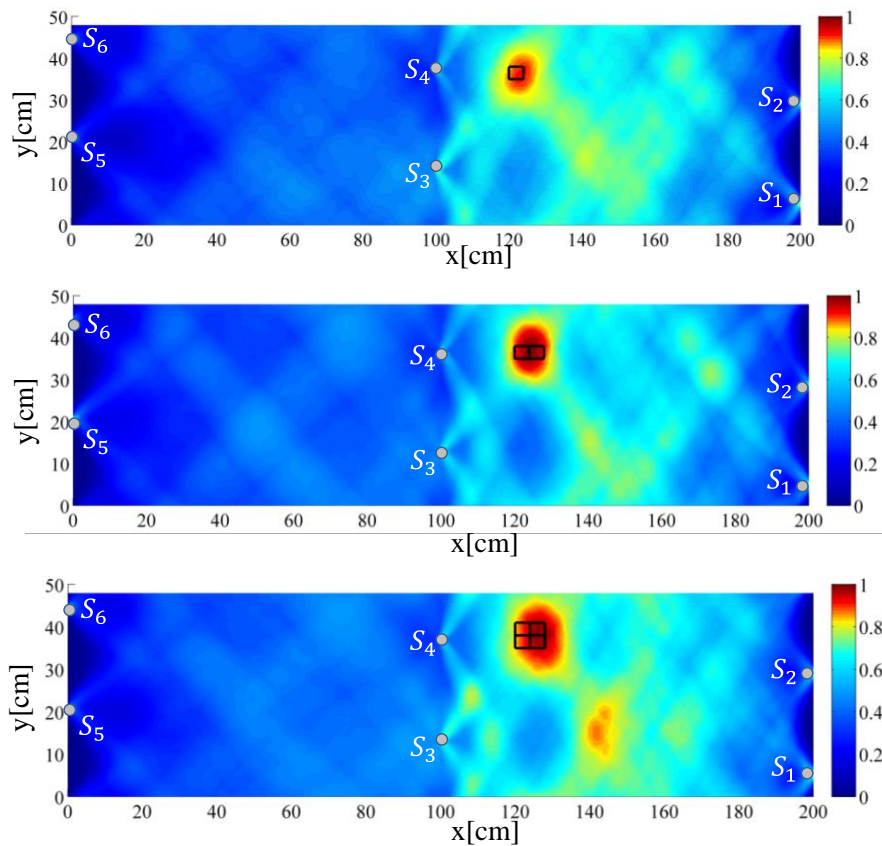


Fig. 9 Reconstructed images using MHUI: (a) corrosion case I, (b) corrosion case II and (c) corrosion case III (Color Online)

Table 1 List of unambiguous independent transducer pairs

Trans./Rec. Pair #	Trans. #	Rec. #
1	1	3
2	1	4
3	1	5
4	1	6
5	2	3
6	2	4
7	2	5
8	2	6
9	3	5
10	3	6
11	4	5
12	4	6

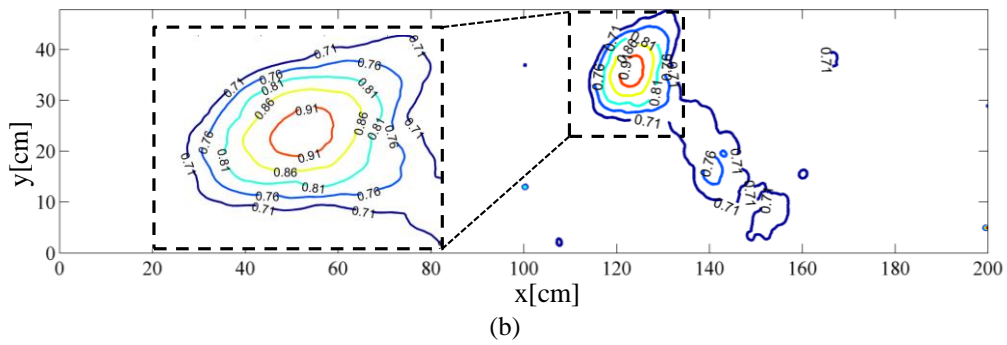
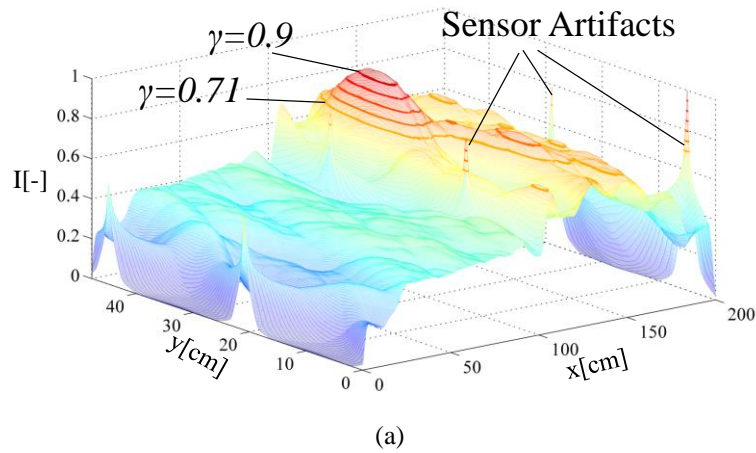


Fig. 10 Image intensity of the corrosion case I (a) different contour levels in 3-D view and (b) contours in 2-D as possible corrosion boundaries

Consider an image associated with the corrosion case I with image intensity $I(x,y)$ (Fig. 9(a)). A number of contours associated with different values of γ can be identified as shown in Fig. 10(a). The projections of each contour line $\bar{\Gamma}_\gamma(x,y)$ in the unwrapped configuration is depicted in Fig. 10(b). It is worth noting the existence of several artifacts at the sensor locations. These artifacts occur due to accumulation of several elliptical shapes with the focal points being at each sensor location. This problem is solved in the image by smoothing the sensor area and eliminating the contour lines associated with these artifacts.

Having $\bar{\Gamma}_\gamma(x,y)$ at a particular level and based on the geometry of the sensor network the portion of each helical path \bar{d}_{kh} that goes inside contour $\bar{\Gamma}_\gamma(x,y)$ can be theoretically determined. For illustrative purpose, \bar{d}_{kh} are shown in Figure 11 with bold gray lines inside the $\bar{\Gamma}_{0.71}(x,y)$. These values were used for solving the objective function in Eq. (13) at gridded values of γ and group wave velocity \bar{V} inside the corrosion patch. A surface plot of the logarithmic values of weighted least square error in Eq. (13) for the corrosion case I, is given in Fig. 12. It can be observed that the objective function is convex, and its minimum value is located at a contour level of 0.987 and wave velocity of 2785.8 m/sec. The centroid and the area of $\bar{\Gamma}_\gamma(x,y)$ indicate the location and corrosion patch size, respectively. Furthermore, one can use the dispersion group velocity to find the remnant thickness associated with the estimated wave velocity \bar{V} inside the corrosion patch. The estimated boundaries $\bar{\Gamma}_\gamma(x,y)$ of the three simulated corrosion patches are shown in Fig. 13. The contour levels γ , area and the location associated with these boundaries and the thickness loss associated with the estimated wave velocity \bar{V} in the corrosion patch are given in Tables 2 and 3 respectively.

The results show a reasonable agreement between the estimated and the actual value of the damage location. However, the corresponding areas are slightly overestimated for case I and II; two are the possible reasons for these errors. First, since the direction of the higher order helical paths going through the damaged area tend to be more vertical, the horizontal dimension of the corrosion patch cannot be accurately captured in the image reconstruction stage.

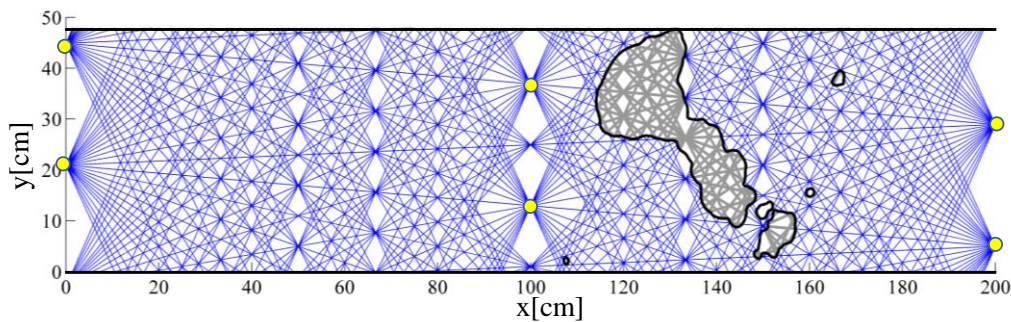


Fig. 11 Example of a contour level for $\bar{\Gamma}_{0.71}(x,y)$ from image of corrosion case I

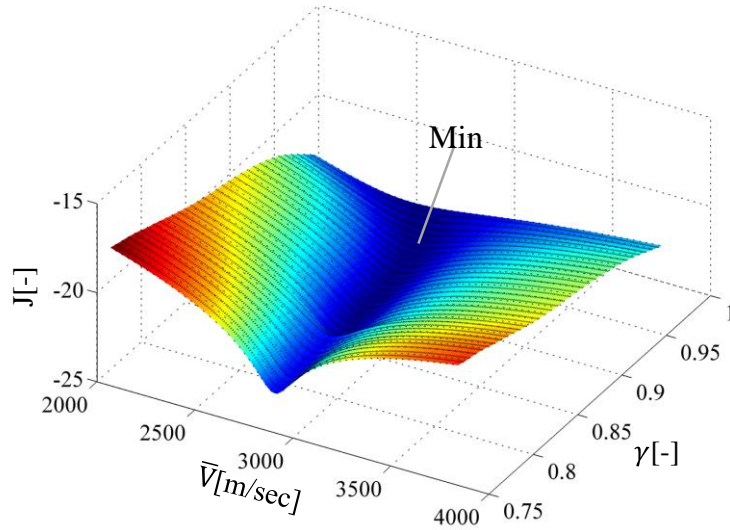


Fig. 12 Error in (13) evaluated at gridded contour level and velocity in the corrosion case I

Table 2 Location Estimation and Area Estimation

Corrosion Stage	I	II	III
γ	0.920	0.948	0.950
*Estimated x [cm]	123.25	124.27	126.54
Exact x [cm]	122	124	124
*Estimated y [cm]	35.72	36.7	38.15
Exact y [cm]	36.42	36.42	37.9
*Estimated Area[cm ²]	13.98	34.81	45.46
Exact Area [cm ²]	12	24	48

Table 3 Thickness Estimation

Corrosion Stage	I	II	III
\bar{V} [m/sec]	2785.8	2702.5	2714.1
Estimated remnant Thickness [mm]	1.58	1.40	1.42
Exact Remnant Thickness [mm]	1.26±0.1	1.26±0.1	1.26±0.1

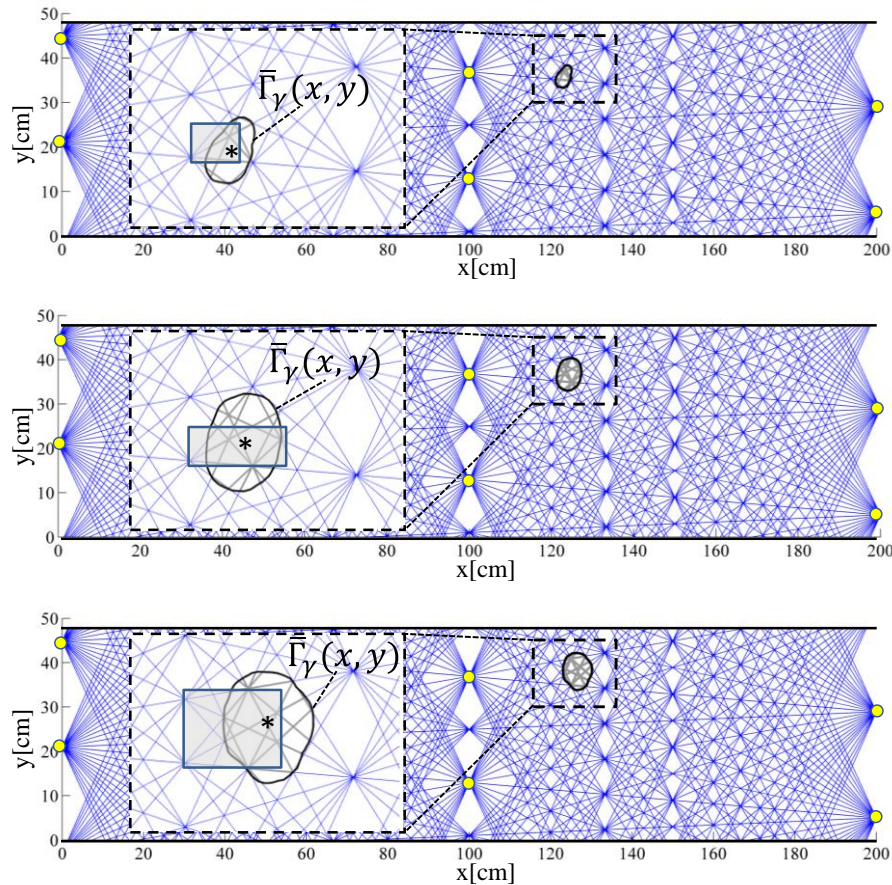


Fig. 13 Quantitative corrosion patch monitoring results. The “*” is at the centroid of the estimated corrosion boundary

Fig. 13(b) shows that the maximum error among the three corrosion cases is related to the case II where the shape of the corrosion patch is rectangular elongated in the horizontal direction. The second reason is related to the violation of the ray theory condition related to the Fresnel zone. Although the characteristic size of the corrosion in all cases is comparable to the wavelength λ , for the corrosion case I and II the size is smaller than the width of the Fresnel zone. Belanger and Cawley (2009) demonstrated that if the damage size is smaller than the width of the first Fresnel zone the area of the damage can be overestimated using A_0 Lamb mode. This problem is due to scattering effects that cause erroneous time delay in the wave packets of rays (helical paths in the vicinity of corrosion patch) that do not pass the corrosion patch. These time delays will appear in the objective function given in Eq. (13) and compromise the estimation of the corrosion boundary. Table III shows the estimated wave velocities and the associated remnant thicknesses for the three simulated corrosion patches. The remnant thicknesses are slightly underestimated. Again as it was shown in Belanger and Cawley (2009) this error is most likely caused by the violation of the ray

theory related to the Fresnel zone. It is worth noting that, although the imaging method exploited in this paper to provide the qualitative image information was the MHUI, other imaging algorithms could be adapted in the same fashion to quantify damage using the image information.

5. Conclusions

In this paper we extended the Multi Helical Ultrasonic Imaging (MHUI) method, recently developed by the authors for locating corrosion damage in cylindrical structures, to provide quantitative information about the corrosion process, including location coordinates, size and remnant thickness. The proposed approach consists of two main stages. In the first stage image information is provided by the MHUI method. In the second stage corrosion characteristics are estimated by solving an optimizing problem. The main advantage of the proposed method is the ability to exploit qualitative image information in order to quantify the extent of the corrosion damage using a low density sensor network. Experiments were carried out on a steel pipe instrumented with six permanently attached piezoelectric disks to validate the proposed approach. Three thickness recesses simulating corrosion patch were considered. Results demonstrated that the proposed method can successfully estimate the location, corrosion area and the remnant thickness with reasonable accuracy and by using a small number of sensors.

Acknowledgments

Funding for this research has been provided by the United States Department of Transportation (DOT), Pipeline and Hazardous Materials Safety Administration's (PHMSA) under the Competitive Academic Agreement Program (CAAP) (#DTPH56-13-H-CAAP03). Any opinions, findings, conclusions or recommendations expressed are those of the author(s) and do not necessarily reflect the views of the PHMSA.

References

- Belanger, P. (2009), Feasibility of thickness mapping, Imperial College London.
- Belanger, P. and Cawley, P. (2008), "Lamb wave tomography to evaluate the maximum depth of corrosion patches", *AIP Conf. Proc.*
- Belanger, P. and Cawley, P. (2009), "Feasibility of low frequency straight-ray guided wave tomography", *NDT & E Int.*, **42**, 113-119. doi: 10.1016/j.ndteint.2008.10.006
- Belanger, P., Cawley, P. and Simonetti, F. (2010), "Guided wave diffraction tomography within the born approximation", *IEEE T. Ultrason Ferr.*, **57**, 1405-1418. doi: 10.1109/TUFFC.2010.1559
- Brondel, D., Edwards, R., Hayman, A. *et al.* (1994), "Corrosion in the Oil Industry", *Oil Rev* 4-18. doi: 10.1021/ie50320a006
- Ciampa, F., Pickering, S., Scarselli, G. *et al.* (2014), "Nonlinear elastic tomography using sparse array measurements", to cite this version 7th Eur. work. struct", *Struct Health. Monit.*, Nantes, Fr., 1878-1885.
- Dehghan-Niri, E. and Salamone, S. (2014), "A multi-helical ultrasonic imaging approach for the structural health monitoring of cylindrical structures", *Struct. Health Monit.*, **14**, 73-85. doi: 10.1177/1475921714548937
- Dehghan-niri, E., Zahrai, S.M. and Mohtat, A. (2010), "Effectiveness-robustness objectives in MTMD

- system design : An evolutionary optimal design methodology”, *Struct Control Heal Monit.*, 218-236. doi: 10.1002/stc
- Flynn, E.B., Todd, M.D., Wilcox, P.D. *et al.* (2011), “Maximum-likelihood estimation of damage location in guided-wave structural health monitoring”, *Proc. R. Soc. A. Math. Phys. Eng. Sci.*, **467**, 2575-2596. doi: 10.1098/rspa.2011.0095
- Gao, H., Shi, Y. and Rose, J.L. (2005), “Guided wave tomography on an aircraft wing with leave in place sensors”, AIP Conf. Proc.
- Hall, J.S., Fromme, P. and Michaels, J.E. (2011), “Ultrasonic guided wave imaging for damage characterization”, *Proceedings of the Airc. Airworth. Sust. Conf.*
- Hinders, M., Malyarenko, E. and McKeon, J. (1998), “Contact scanning Lamb wave tomography”, *J. Acoust. Soc. Am.*, **104**, <http://dx.doi.org/10.1121/1.423524>.
- Huthwaite, P., Ribichini, R., Cawley, P. and Lowe, M.J.S. (2013), “Mode selection for corrosion detection in pipes and vessels via guided wave tomography”, *IEEE T. Ultrason Ferroelectr Freq Control* **60**, 1165-1177. doi: 10.1109/TUFFC.2013.2679
- Huthwaite, P. and Simonetti, F. (2013), “High-resolution guided wave tomography”, *Wave Motion*, **50**, 979-993. doi: 10.1016/j.wavemoti.2013.04.004
- Jansen, D.P. and Hutchins, D.A. (1990), “Wave tomography”, *Ultrason. Symp.*, 1017-1020.
- Kolda, T.G., Lewis, R.M. and Torczon, V. (2003), “Optimization by direct search: New perspectives on some classical and modern methods”, *SIAM Rev.*, **45**, 385-482. doi: 10.1137/S003614450242889
- Leonard, K.R. and Hinders, M.K. (2003), “Guided wave helical ultrasonic tomography of pipes”, *J. Acoust. Soc. Am.*, **114**, 767. doi: 10.1121/1.1593068
- Leonard, K.R. and Hinders, M.K. (2005a), “Lamb wave tomography of pipe-like structures”, *Ultrasonics*, **43**, 574-583. doi: 10.1016/j.ultras.2004.12.006
- Leonard, K.R. and Hinders, M.K. (2005b), “Multi-mode Lamb wave tomography with arrival time sorting”, *J. Acoust. Soc. Am.*, **117**, 2028. doi: 10.1121/1.1867792
- Li, J. and Rose, J.L. (2006), “Natural beam focusing of non-axisymmetric guided waves in large-diameter pipes”, *Ultrasonics*, **44**, 35-45. doi: 10.1016/j.ultras.2005.07.002
- Lu, Y. and Michaels, J.E. (2005), “A methodology for structural health monitoring with diffuse ultrasonic waves in the presence of temperature variations”, *Ultrasonics*, **43**, 717-731. doi: 10.1016/j.ultras.2005.05.001
- Nagy, P.B., Simonetti, F. and Instanes, G. (2014), “Corrosion and erosion monitoring in plates and pipes using constant group velocity Lamb wave inspection”, *Ultrasonics*, **54**, 1832-1841. doi: 10.1016/j.ultras.2014.01.017
- Pierce, A.D. and Kil, H.G. (1990), “Elastic wave propagation from point excitations on thin-walled cylindrical shells”, *J. Vib. Acoust.*, **112**, 399. doi: 10.1115/1.2930524
- Qing, X.P., Beard, S., Shen, S.B. *et al.* (2009) “Development of a real-time active pipeline integrity detection system”, *Smart Mater. Struct.*, **18**, 115010. doi: 10.1088/0964-1726/18/11/115010
- Willey, C.L., Simonetti, F., Nagy, P.B. and Instanes, G. (2014), “Guided wave tomography of pipes with high-order helical modes”, *NDT & E Int.*, **65**, 8-21. doi: 10.1016/j.ndteint.2014.03.010
- Zhao, X., Gao, H., Zhang, G. *et al.* (2007), “Active health monitoring of an aircraft wing with embedded piezoelectric sensor/actuator network: I. Defect detection, localization and growth monitoring”, *Smart Mater Struct.*, **16**, 1208-1217. doi: 10.1088/0964-1726/16/4/032